JOURNAL OF SPACECRAFT AND ROCKETS
Vol. 43, No. 3, May–June 2006

Propulsion Requirements for Drag-Free Operation of Spacecraft in Low Earth Orbit

Brian St. Rock,[*] John J. Blandino,[†] and Michael A. Demetriou[‡]
Worcester Polytechnic Institute, Worcester, Massachusetts 01609

The use of drag-free spacecraft in low Earth orbit has the potential for enabling gravitational surveys with substantial improvement in sensitivity over the Gravity Recovery and Climate Experiment (GRACE) mission. We evaluate the required thrust envelope, maximum thruster dynamic response, and ΔV for a 5-year drag-free mission over a range of low-Earth-orbit altitudes (150–450 km). The analysis uses the Jacchia–Roberts atmospheric density model and an adaptive, proportional-derivative control algorithm in which full-state error feedback is used to command compensation of disturbing forces by the thrusters. The actuator (thruster) control resolution and control loop frequency are limited to 0.1 μN and approximately 0.8–31 Hz, respectively. Detailed results at 450 km show that the thrust ranges from 10 to 145 μN, the maximum thruster dynamic response is 5.9 μN/s, and the ΔV for a 5-year mission is approximately 20 m/s. Although drag is the dominant disturbance force, the disturbance due to solar radiation pressure is on the same order at 450 km. At 250 km, the thrust ranges from 1.3 to 5.4 mN, the maximum thruster dynamic response is 6.9 μN/s, and the ΔV for a 5-year mission increases to 865 m/s. We consider seven different electric propulsion options as possible candidates for this mission. The selection will be strongly dependent on the altitude, which for the altitudes considered, increases the required thrust (and power) through several orders of magnitude. We conclude that existing thruster technology should be adequate for altitudes above 250 km, but below this the required power and ΔV for a 5-year mission may be prohibitive.

Nomenclature

$A_\odot$ = cross-sectional, sun-facing area, m^2
a = semimajor axis of orbit, km
$\boldsymbol{a}_d$ = acceleration due to atmospheric drag, km/s^2
$\boldsymbol{a}_{\mathrm{ns}}$ = acceleration due to aspherical geopotential, km/s^2
$\boldsymbol{a}_s$ = acceleration due to solar radiation pressure, km/s^2
$a_\oplus$ = mean distance from sun to Earth, km
C_b = ballistic coefficient, kg/m^2
C_d = drag coefficient
C_R = reflectivity coefficient
c = drag parameter, m^{-1}
$\hat{c}$ = adaptive estimate, m^{-1}
$\hat{c}_o$ = initial adaptive estimate, m^{-1}
$\tilde{c}$ = drag parameter error, m^{-1}
$\hat{\boldsymbol{e}}_v$ = velocity unit vector
i = inclination of orbital plane, deg
K_D = derivative gain matrix, s^{-1}
K_P = proportional gain matrix, s^{-2}
m = spacecraft mass, kg
$P_\odot$ = mean solar radiation pressure at 1 AU, N/m^2
$\boldsymbol{r}$ = spacecraft position vector, km
$\dot{\boldsymbol{r}}$ = spacecraft velocity vector, km/s
$\ddot{\boldsymbol{r}}$ = spacecraft acceleration vector, km/s^2
$\boldsymbol{r}_\odot$ = sun-to-spacecraft position vector, km
$\boldsymbol{u}$ = control acceleration vector, km/s^2
V = Lyapunov function
$\boldsymbol{v}_{\mathrm{rel}}$ = velocity of spacecraft relative to atmosphere, km/s
Γ = adaptive gain
γ = secondary velocity error gain
$\delta\boldsymbol{r}$ = position error, m
$\delta\dot{\boldsymbol{r}}$ = velocity error, m/s
$\delta\ddot{\boldsymbol{r}}$ = state acceleration error, m/s^2
ε = eccentricity
ζ = damping coefficient
$\lambda_{\min}(\cdot)$ = minimum eigenvalue of a matrix
μ = Earth's gravitational parameter, km^3/s^2
ν = true anomaly, deg
ρ = atmospheric density, kg/m^3
χ = percentage of solar illumination
Ω = right ascension of the ascending node, deg
ω = argument of perigee, deg
ω_n = natural frequency of simple harmonic oscillator, Hz
$\omega_\oplus$ = angular velocity of the Earth's rotation, rad/s

I. Introduction

A. Drag-Free Missions

THE continued development of thrusters capable of delivering thrust in the range from 1 to 100 μN with a control resolution of 0.1 μN has opened a number of possibilities for spacecraft formation control. Field emission electric propulsion (FEEP)[1,2] and colloid[3] thrusters are among the candidate technologies. In the United States, colloid thrusters are under development and are scheduled to be flown on NASA's ST7 mission as part of the Disturbance Reduction System (DRS) experiment. This mission is designed to validate micronewton (colloid) thrusters (Busek Co., Inc.) and gravitational reference sensors (GRS). The successful space validation of these technologies would support their eventual use on other so called "drag-free" missions. In this context, "drag-free" refers to the continuous cancellation of external disturbances on the spacecraft surrounding a reference or proof mass that, in principle, is following a trajectory subject only to gravitational forces. Disturbance forces that need to be compensated for will include solar radiation pressure and atmospheric drag. A number of missions could benefit from a successful demonstration of the DRS. These include heliocentric orbital missions such as the Laser Interferometer Space Antenna (LISA)[4] and the Micro-Arcsecond X-Ray Imaging (MAXIM) mission.

A key to drag-free operation is the GRS. For LISA, this sensor consists of a proof mass: a cube made of a gold–platinum alloy

---

Received 28 January 2005; revision received 24 June 2005; accepted for publication 20 July 2005. Copyright © 2005 by the authors. Published by the American Institute of Aeronautics and Astronautics, Inc., with permission. Copies of this paper may be made for personal or internal use, on condition that the copier pay the $10.00 per-copy fee to the Copyright Clearance Center, Inc., 222 Rosewood Drive, Danvers, MA 01923; include the code 0022-4650/06 $10.00 in correspondence with the CCC.

[*] Graduate Student, Mechanical Engineering Department, 100 Institute Road. Student Member AIAA.

[†] Assistant Professor, Mechanical Engineering Department, 100 Institute Road. Senior Member AIAA.

[‡] Associate Professor, Mechanical Engineering Department, 100 Institute Road. Senior Member AIAA.

enclosed within a set of capacitive position sensors. These sensors provide position and attitude information for the proof mass relative to the sensor housing (and spacecraft) with accuracy on the order of nanometers and tens of nanoradians, respectively.[4] In operation as an accelerometer, the proof mass position can be maintained through electrostatic forces applied by the surrounding electrodes. The force needed to maintain its position provides feedback to a controller that can command the required thrust level provided by the propulsion system on the spacecraft.

The U.S. Navy TRIAD spacecraft provided the first demonstration of drag-free control in 1972, and the needed technology has continued to evolve as a result of development supporting NASA's Gravity Probe B[5] and LISA missions. The MICROSatellite with drag Control for the Observation of the Equivalence Principle (MICROSCOPE) is a Centre National d'Etudes Spatiales (CNES) mission currently scheduled for launch in 2008 (Ref. 6). MICROSCOPE is designed to use FEEP thrusters to provide a drag-free environment for the spacecraft in a 700-km sun-synchronous orbit. In addition to basic science, the mission will qualify technology needed for drag-free operation in Earth orbit. Drag-free operation in Earth orbit is much more demanding than in a heliocentric, Earth-trailing orbit because of the magnitude of the atmospheric drag force. A relatively near-term Earth-orbiting drag-free mission that is under consideration is a follow-on to the Gravity Recovery And Climate Experiment (GRACE) mission.[7]

Previous studies, conducted at NASA Goddard in conjunction with Honeywell Space Systems, have investigated, in detail, drag-free mission architectures.[8] Along with detailed trade studies between drag-free (continuous) control systems and traditional (impulsive) control approaches, these studies determined that continuous cancellation of drag is significantly more efficient (from a ΔV standpoint) than intermittent, high-thrust maneuvers. Savings in fuel usage of more than 50% can be realized in comparison with occasional impulsive orbit corrections.[8] These studies further validate the drag-free control concept as a mission-enabling architecture.

B. GRACE and a Possible Drag-Free Follow-On Mission

The GRACE mission[9,10] consists of two spacecraft designed to produce a highly accurate mapping of the Earth's gravity field. The two GRACE spacecraft[10] are three-axis stabilized, and are nearly identical, with a mass at launch of 487 kg and dimensions approximately $1.9 \times 3.1 \times 0.72$ m. The spacecraft were launched in March 2002 into a near-polar 88.5-deg inclination, 500-km orbit. The key to achieving the science objectives for GRACE is a microwave ranging instrument[9] that provides very accurate measurements of the separation between the two spacecraft. Variations in the Earth's mass distribution affect each of the spacecraft at slightly different phases of its orbit. The variations in the gravity field can in turn be correlated with variations in the range between the spacecraft. In addition, each spacecraft also carries a high-precision three-axis accelerometer and global positioning system receiver so that effects of nongravitational acceleration can be accounted for and gravity measurements identified with coordinates in a terrestrial reference frame.[9]

The spacecraft began the mission with an in-track separation of approximately 170 km, which, due to the differential drag acceleration, increases to approximately 270 km over 30–60 days. Periodic maintenance of the attitude and relative separation is accomplished through the use of 10- and 40-mN cold gas thrusters, respectively. Six 30-A/m^2 magnetic torque rods are used to make fine adjustments to the satellite's orientation,[10] thereby reducing the amount of thrust required for attitude control. The drag force will lower the orbit of the spacecraft from 500 to 300 km over the course of the 5-year mission. Operation of a "GRACE-like" mission at lower altitude would result in a significant increase in measurement sensitivity. A drag-free follow-on mission to GRACE has been proposed with this goal in mind.[7]

C. Scope of the Present Study

The primary goal of the present study is to assess the propulsion requirements for a drag-free GRACE-like mission. Because a detailed spacecraft definition for the GRACE follow-on mission is not available at this time, we assume spacecraft and orbital parameters (with the exception of altitude) corresponding to GRACE as a basis for the analysis. Detailed analysis is performed for three altitudes: 450, 250, and 150 km. We evaluate the maximum and minimum thrust level as well as the maximum dynamic response from the thrusters as a function of altitude over the range 150–450 km. Also, a realistic 0.1-μN thrust control resolution is included into the propagator dynamics to better simulate the available technology.

Our first objective is to determine the maximum thrust level that must be provided by an actuator (thruster) system to provide drag compensation to maintain both altitude and relative separation. The second objective is to assess the dynamic response that would be required from the thrusters. This requirement is directly linked to the control strategy employed, to the atmospheric density model used, and also to the orbital period of the spacecraft. An adaptive control strategy is employed along with the Jacchia–Roberts (J71) density profile, calculated using FreeFlyer (AI solutions) software and input into a propagator developed in MATLAB® (MathWorks). The third objective is to calculate the total ΔV required to provide drag-free operation over a five-year mission.

The paper is organized as follows. Section II describes the coordinate systems used, as well as the force model used for the simulations. This is followed in Sec. III by a description of the closed-loop, full-state feedback controller used in the analysis. Section IV presents the results of the analysis for four cases considered in detail. In addition, the sensitivity of required thrust, dynamic response, and ΔV for altitudes of 150–450 km is presented. Section V presents an initial evaluation of possible thruster options which can meet the requirements. This is followed by some conclusions in Sec. VI. A stability analysis of the controller is provided in the Appendix.

II. Spacecraft Dynamics

A. Reference Frames

The two coordinate frames that are shown in Fig. 1 and used extensively in this study are the inertial geocentric-equatorial (GCI) and a satellite-centered rotating frame (NTW). The GCI reference frame is used to define the equations of motions, the state error inputs into the control law, and the calculated thrust accelerations. The NTW frame[11] has its origin at the center of mass of the floating proof mass. The along-track, or T axis, of this reference frame is collinear with the velocity vector of the satellite. The cross-track, or W axis, is perpendicular to the orbital plane and is collinear with the angular momentum vector of the orbit. Note that for a circular orbit, the N axis is just a radial extension of a spacecraft's position vector. In this study, the spacecraft occupy orbits with a slight eccentricity, so the N axis of the NTW frame is slightly out of alignment with the satellite's position vector. Whereas the controller will calculate the required thrust acceleration in the GCI frame (based on the GCI state error inputs), the applied thrust will be reported in the local spacecraft body-fixed frame (assumed to coincide with the rotating NTW frame) to more accurately portray thruster mounting on the spacecraft.

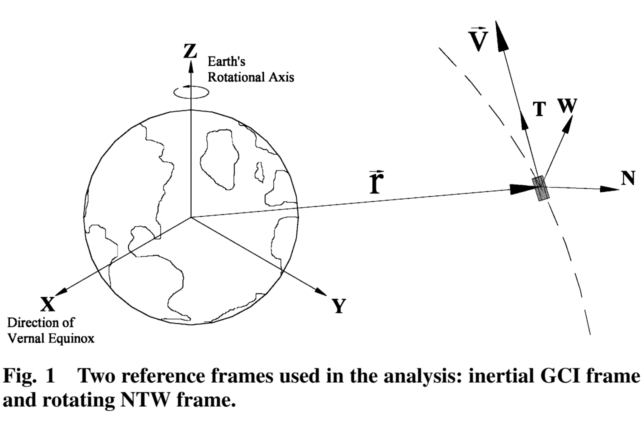

Fig. 1 Two reference frames used in the analysis: inertial GCI frame and rotating NTW frame.

B. Orbital Perturbations

For a spacecraft in low Earth orbit (LEO), the dominant nongravitational orbital perturbations of satellite motion will be from atmospheric drag and solar radiation pressure. For the altitudes considered in the present study, solar radiation pressure is never greater than half the drag perturbation.

1. Atmospheric Drag Model

Drag is a nonconservative force that acts in the direction opposite to the spacecraft velocity vector, thus reducing the satellite's total energy. This reduction in system energy results in a gradual deorbiting of the spacecraft. The drag acceleration on an orbiting body is modeled as[11,12]

$$\boldsymbol{a}_d(t) = -\frac{1}{2}\left(\frac{C_d A \rho}{m}\right)\|\boldsymbol{v}_{\text{rel}}(t)\|^2 \frac{\boldsymbol{v}_{\text{rel}}(t)}{\|\boldsymbol{v}_{\text{rel}}(t)\|} \tag{1}$$

where the quantity $m/C_d A$ is the ballistic coefficient (C_b). This quantity provides a measure of the susceptibility of a spacecraft to drag forces. In Eq. (1), the relative velocity $\boldsymbol{v}_{\text{rel}}$ is the velocity of the spacecraft with respect to the atmosphere. Assuming that the atmosphere corotates with the angular velocity of the Earth[12] ($\omega_\oplus = 7.3 \times 10^{-5}$ rad/s), this relative velocity is given by

$$\boldsymbol{v}_{\text{rel}}(t) = \boldsymbol{v}(t) - \omega_\oplus \times \boldsymbol{r}(t) \tag{2}$$

Although no detailed wind model has been assumed in the calculations, the impact of winds on the maximum thrust level is discussed in the results section for case 3 (250-km altitude).

By grouping together the velocity terms in Eq. (1), the drag acceleration can be rewritten in compact form as the product of the square of the relative speed, the velocity unit vector $\hat{\boldsymbol{e}}_v$, and a scalar:

$$\boldsymbol{a}_d(t) = c\hat{\boldsymbol{e}}_v(t)\|\boldsymbol{v}_{\text{rel}}(t)\|^2 \tag{3}$$

where

$$c = \rho\left(\frac{C_d A}{2m}\right) = \frac{\rho}{2C_b}, \qquad \hat{\boldsymbol{e}}_v(t) = -\frac{\boldsymbol{v}_{\text{rel}}(t)}{\|\boldsymbol{v}_{\text{rel}}(t)\|}$$

In this study the scalar quantity c will be referred to as the *drag parameter*. This notation will simplify the subsequent discussion and stability analysis of the control system.

2. Atmosphere Model

Any drag-free simulation will be highly sensitive to the drag model used. Although standard atmosphere models perform reasonably well in predicting fuel consumption (ΔV) over mission lifetime, they do not provide an accurate picture of the thrust profile needed for drag-free control due to the omission of time-dependent density fluctuations. These fluctuations can be severe, posing significant challenges for the dynamic response of a thruster. The atmosphere model used to calculate the drag acceleration for the present study was the Jacchia–Roberts density model. This is a version of Jacchia's 1971 atmosphere model with changes made to the exospheric temperature profile to enable analytic integration of the diffusion equation.[13] Variations in the Jacchia–Roberts model are caused by changes in the altitude of the spacecraft, which in this study are a result of the eccentric orbit. Additionally, density variations predicted by this model are caused by temporal effects on the exospheric temperature (caused by diurnal, semiannual, and seasonal latitudinal effects). These time-dependent effects are parameterized by changes in the mean solar activity ($F_{10.7}$ index) and geomagnetic index a_p. The Jacchia–Roberts model then modifies the thermospheric density based on these time-dependent effects, as well as the spacecraft's position.[11]

The time dependence of the $F_{10.7}$ flux and geomagnetic index requires that specific dates be used as inputs into the simulation. The start date for the calculations was chosen to be 1 January 2010. Although somewhat arbitrary, this date places the 5-year mission in the middle of solar cycle 24 (spanning from 2005 to 2016), ensuring that spacecraft will pass through some period of maximum solar activity (and hence an "unkind" atmosphere). Solar flux prediction files (Schatten files) are used to accurately forecast these values over an entire 11-year solar cycle.[14] Mean $F_{10.7}$ and a_p values with nominal phasing were used for the predictions in this study. Comparisons between Jacchia71 and newer atmosphere models have been made previously by Chao et al.[15] (among others). The results of that work suggest that the Jacchia71 model overpredicts the atmospheric density by 9 to 22%. Therefore, the Jacchia–Roberts atmosphere provides a reasonably conservative baseline for identifying propulsion requirements.

3. Solar Radiation Pressure

Solar radiation pressure (SRP) on a spacecraft is caused by absorbed and reflected radiation that imparts a negative acceleration on the spacecraft, thereby dissipating energy from the satellite. The effect of this force is to degrade the orbit by causing a gradual decrease in the spacecraft's semimajor axis. The component of this acceleration in the sun-to-satellite direction is given by[12]

$$\boldsymbol{a}_s(t) = -\chi P_\odot \frac{a_\oplus^2}{\|\boldsymbol{r}_\odot(t)\|^2} \frac{A_\odot(t) C_R}{m} \frac{\boldsymbol{r}_\odot(t)}{\|\boldsymbol{r}_\odot(t)\|} \tag{4}$$

The area $A_\odot(t)$ is the cross-sectional area of the spacecraft exposed to the solar flux. This area will change with time due to the satellite orbiting the Earth, the Earth orbiting the sun, and the orbital plane of the satellite regressing due to nonspherical Earth perturbations. The term ${a_\oplus}^2/\|\boldsymbol{r}_\odot(t)\|^2$ accounts for annual variations in the mean solar radiation pressure at 1 AU ($P_\odot = 4.56 \times 10^{-6}$ N/m^2) caused by the eccentricity of the Earth's orbit around the sun. The term χ is defined as the percentage of the total solar flux that is actually imparted onto the spacecraft. Here, $\chi = 1$ when fully illuminated, $\chi = 0$ when fully eclipsed, and $0 < \chi < 1$ in the penumbra.

This form of the equation assumes that the spacecraft area $A_\odot(t)$ lies normal to the incoming solar flux so that the imparted acceleration from an assumed diffuse surface (defined by the reflectivity coefficient, C_R) acts along the sun-to-satellite unit vector, $-\boldsymbol{r}_\odot(t)$. This vector is computed by FreeFlyer and input into the MATLAB simulation. Because of the relatively simple planar surfaces on the GRACE spacecraft, there will be no secondary irradiation. Hence, the solar flux reflected off the spacecraft surface will not be incident on another part of the spacecraft, simplifying the SRP model by eliminating the need for any complex ray-tracing algorithms.

4. Additional Disturbances

Other nonconservative disturbing forces that will act on the spacecraft will be those from Earth radiation pressure (albedo) and thermal reradiation. These two disturbances are higher-order effects, an order of magnitude lower than that of atmospheric drag, even at the highest altitude modeled in this study. Worst case albedo and thermal reradiation forces are approximately <5 and <2 μN, respectively, and are negligible when compared to the disturbing force of drag. Also, albedo force is extremely difficult to model accurately, varying with surface/atmospheric properties of the Earth (oceans, icecaps, cloudcover, etc.). For these reasons, they were not included in the model. It is also noted that albedo force acts radially outward from the Earth, which by definition of the NTW reference frame, is nearly orthogonal to the spacecraft's velocity vector. Therefore, the thrusters providing the largest acceleration component would not be stressed further by the presence of an albedo force. Also neglected in the force model are any magnetic field forces on charged components of the spacecraft (i.e., Lorentz forces). Although these nongravitational accelerations are important for accurate gravity field mapping and orbit determination, they do not add any significant additional requirements from a propulsion system standpoint.

III. Controller Description

A. Equations of Motion

The target trajectory $\boldsymbol{r}_t(t)$ is an idealized orbit with no drag and represents the solution to the equation of motion perturbed only by

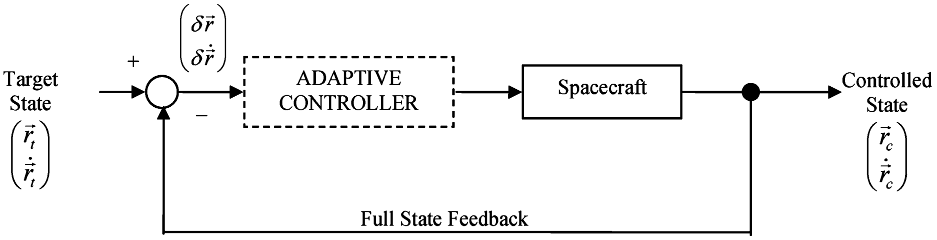

Fig. 2 Block diagram of the closed-loop feedback control system. The controller is designed assuming the availability of full-state feedback.

the nonspherical geopotential:

$$\ddot{\boldsymbol{r}}_t(t) = -\mu\frac{\boldsymbol{r}_t(t)}{\|\boldsymbol{r}_t(t)\|^3} + \boldsymbol{a}_{\mathrm{ns},t} \tag{5}$$

With this definition for the spacecraft's desired target orbit, the controller will eliminate not only periodic in-track drift between the two spacecraft due to differential nongravitational disturbances, but will also prevent secular disturbances (orbit decay) that would lead to deorbiting. Essentially, the orbit is "raised" continuously as the controller fights drag.

The "controlled" spacecraft trajectory $\boldsymbol{r}_c(t)$ is subject to atmospheric drag and a control acceleration $\boldsymbol{u}(t)$ and represents the solution to the equation of motion

$$\ddot{\boldsymbol{r}}_c(t) = -\mu\frac{\boldsymbol{r}_c(t)}{\|\boldsymbol{r}_c(t)\|^3} + \boldsymbol{u}(t) + \boldsymbol{a}_d(t) + \boldsymbol{a}_{\mathrm{ns},c} \tag{6}$$

where $\boldsymbol{a}_{\mathrm{ns}}$ represents the perturbing acceleration due to a nonspherical gravity potential. We use a simplified model by Vallado[11] for the zonal harmonic (J_2–J_6) acceleration terms.

The equations of motion can now be combined and written in terms of the difference in states (i.e., the state acceleration error) as follows:

$$\begin{aligned}\delta\ddot{\boldsymbol{r}}(t) &= \ddot{\boldsymbol{r}}_c(t) - \ddot{\boldsymbol{r}}_t(t)\\ &= \mu\left(\frac{\boldsymbol{r}_t(t)}{\|\boldsymbol{r}_t(t)\|^3} - \frac{\boldsymbol{r}_c(t)}{\|\boldsymbol{r}_c(t)\|^3}\right) + \boldsymbol{a}_d(t) + \boldsymbol{u}(t)\end{aligned} \tag{7}$$

where the differential, nonspherical Earth acceleration goes to zero (i.e., $\boldsymbol{a}_{\mathrm{ns},t} = \boldsymbol{a}_{\mathrm{ns},c}$). This assumption is valid if the state errors are kept small and the proof mass is positioned at the center of mass of the satellite.

B. Control Acceleration

In the control implementation, the "errors" to be controlled are based on the difference between the satellite's actual position and velocity (state vector) and a "target" state (also known as the reference model) defined as the natural orbit of the proof mass, which is subject only to gravitational acceleration. It is assumed that state data for both the proof mass and spacecraft is available for controller design and therefore $\delta\boldsymbol{r}(t)$ and $\delta\dot{\boldsymbol{r}}(t)$ can readily be generated. The control strategy employed here is designed to use the state information to perform partial state feedback linearization. In this case, the control acceleration term $\boldsymbol{u}(t)$ will include terms that cancel out the nonlinearities in Eq. (7), and change the closed-loop error dynamics to that of uncoupled single-degree-of-freedom (second-order) systems (i.e., implement feedback linearization). The control acceleration is calculated from

$$\begin{aligned}\boldsymbol{u}(t) = &-\mu\left(\frac{\boldsymbol{r}_t(t)}{\|\boldsymbol{r}_t(t)\|^3} - \frac{\boldsymbol{r}_c(t)}{\|\boldsymbol{r}_c(t)\|^3}\right) - [K_P]\delta\boldsymbol{r}(t)\\ &- [K_D]\delta\dot{\boldsymbol{r}}(t) - \hat{c}(t)\hat{\boldsymbol{e}}_v(t)\|\dot{\boldsymbol{r}}_c(t)\|^2\end{aligned} \tag{8}$$

where the proportional and derivative gain matrices $[K_P]$ and $[K_D]$ are $[3 \times 3]$ diagonal matrices. Consistent with the assumption that the full spacecraft state is known, $\hat{\boldsymbol{e}}_v(t)\|\dot{\boldsymbol{r}}_c(t)\|^2$ defines a known vector. However, because the magnitude of the drag parameter and relative velocity $\boldsymbol{v}_{\mathrm{rel}}$ cannot be known a priori (due to uncertainties with respect to the atmospheric density, wind velocity, drag coefficient, and frontal cross-sectional area), a time-varying scalar $\hat{c}(t)$ is introduced, which represents an adaptive, or "on-line," estimate of the actual drag parameter that was defined in Eq. (3). This scalar makes the last term in Eq. (8) approximately cancel the drag, which is known to be a function of the atmospheric density, the spacecraft's physical properties, and the orbital speed relative to the atmosphere (since $\boldsymbol{v}_{\mathrm{rel}} \approx \dot{\boldsymbol{r}}_c$).

Whereas the controller shown in the block diagram of Fig. 2 uses the position error $\delta\boldsymbol{r}$ in the feedback linearizing portion, the adaptive component (which attempts to eliminate the effects of the drag acceleration) and the linear component (which results in a linear, damped, second-order, closed-loop system) use full state information. In the majority of control applications, access to uncorrupted full-state measurements is seldom possible (i.e., only $\delta\boldsymbol{r}$ may be available from the GRS). Thus, one has to resort to consideration of adaptive nonlinear observers that estimate both the velocity error vector, $\delta\dot{\boldsymbol{r}}$, and the unknown drag parameter, $\hat{c}$. In this analysis we make the assumption of uncorrupted full-state measurements to establish a baseline for future comparison. Uncertainty in the position error information will be included in future analysis to more realistically model the information available from actual GRS hardware. Additionally, we assume linear actuator dynamics that produce no variations (additional errors) between the commanded and actual thrust. This assumption simplifies the controller, as the major objective of this work is to establish the required propulsion requirements for drag-free operation. In a future study that will concentrate heavily on the preceding control aspects, the nonlinear actuator dynamics will also be considered in the control design.

The equations of motion for the controlled and target spacecraft can now be combined into a single expression written in terms of the state acceleration error:

$$\delta\ddot{\boldsymbol{r}}(t) = -[K_D]\delta\dot{\boldsymbol{r}}(t) - [K_P]\delta\boldsymbol{r}(t) + \left(\boldsymbol{a}_d(t) - \hat{c}(t)\hat{\boldsymbol{e}}_v(t)\|\dot{\boldsymbol{r}}_c(t)\|^2\right) \tag{9}$$

or in the more familiar form of a vector second-order system:

$$\delta\ddot{\boldsymbol{r}}(t) + [K_D]\delta\dot{\boldsymbol{r}}(t) + [K_P]\delta\boldsymbol{r}(t) = \left(\boldsymbol{a}_d(t) - \hat{c}(t)\hat{\boldsymbol{e}}_v(t)\|\dot{\boldsymbol{r}}_c(t)\|^2\right) \tag{10}$$

Recognizing that $\boldsymbol{a}_d(t) = c\hat{\boldsymbol{e}}_v(t)\|\dot{\boldsymbol{r}}_c(t)\|^2$, it is seen that when $\hat{c}(t) = c$, the solution to the state error equation goes to zero exponentially. Because the true value of the drag parameter is not known, the controller uses information about the state errors and its known dependence on the vector $\hat{\boldsymbol{e}}_v(t)\|\dot{\boldsymbol{r}}_c(t)\|^2$ to continuously adapt the value of the estimated drag parameter, $\hat{c}(t)$. The time rate of change of the adaptive estimate that is used to calculate an updated estimate for this scalar is

$$\frac{\mathrm{d}}{\mathrm{d}t}\hat{c}(t) = -\Gamma(\gamma\delta\dot{\boldsymbol{r}}(t) + \delta\boldsymbol{r}(t))^T\hat{\boldsymbol{e}}_v(t)\|\dot{\boldsymbol{r}}_c(t)\|^2, \qquad \hat{c}(0) = \hat{c}_o \tag{11}$$

where γ is some positive multiplier (secondary velocity error gain), $\hat{c}_o$ is the initial guess of the drag parameter, and Γ acts as an accelerating multiplier that affects the speed of the adaptation (i.e., an adaptive gain). This is an especially important parameter during the initialization period, when the difference between the actual drag parameter and the adaptive estimate is most likely at its maximum. The actual magnitude of this initial parameter error will depend on the accuracy of $\hat{c}_o$.

Table 1 Control parameters used in all simulations

Parameter	Value
ω_n	0.690 Hz
ζ	0.700
Γ	1.55×10^{-4}
γ	1.0001
k_p	$0.4761\ \mathrm{s}^{-2}$
k_d	$0.9660\ \mathrm{s}^{-1}$

C. Gain Calculation

The control acceleration presented in Eq. (8) has both nonlinear and linear components. By canceling the nonlinear dynamics terms in Eq. (7), we are left with only a linear PD-type controller. Therefore, by the proper choice of the feedback matrix gains K_P and K_D, we may ensure that $\delta\boldsymbol{r}$ and $\delta\dot{\boldsymbol{r}}$ will go to zero exponentially. The linear system that results from the removal of the nonlinear term is the equation of a second-order, simple harmonic oscillator in each direction, given by

$$\ddot{r}_i + 2\zeta\omega_n\dot{r}_i + \omega_n^2 r_i = 0, \qquad i = x, y, z \tag{12}$$

The gain coefficients for this linear control component can be found from the roots of this expression, which take the form

$$K_D = k_d[I_{3x3}], \qquad K_P = k_p[I_{3x3}]$$

$$k_d = 2\zeta\omega_n, \qquad k_p = \omega_n^2 \tag{13}$$

In these expressions, ζ is the damping coefficient, and ω_n is the natural frequency of correction. In general, the greater the natural frequency of the system, the less time the errors have to accumulate, thus lowering the magnitude of state errors. Therefore, a high-frequency system is important to lowering the applied thrust demanded by the controller. Too high a frequency, however, can create instabilities because the controller tends to overreact to state errors. In practice, the maximum bandwidth of the thruster and the sampling frequency will place an upper bound on the value of ω_n. The damping coefficient was chosen to be $\zeta = 0.7$. This choice of damping aids in mitigating any excessive thrust oscillations that could result from underdamped motion.

Along with the PD gains, two additional gains are present in the adaptive estimate law of Eq. (11): the adaptive gain Γ and the secondary velocity error gain γ. The value for γ was chosen to be only slightly greater than the lower bound [given by Eq. (A7) in the Appendix] to place more emphasis on the position errors. Also, the adaptive gain Γ was chosen through a limited, iterative process. Additional tuning can be employed prior to or during the mission to achieve optimum values for these input parameters. The control inputs used for all cases in this study are reported in Table 1.

IV. Results and Discussion

A. Problem Description

1. *Spacecraft Properties*

As described in the Introduction, the mission investigated for this study was based on a proposed drag-free GRACE follow-on. Because of the lack of information on the potential spacecraft design to be used on a GRACE follow-on mission, the spacecraft geometry assumed in this study is identical to that of the GRACE spacecraft. Table 2 summarizes the assumed spacecraft properties and the initial orbital parameters. The drag area is the frontal cross-sectional area (assumed constant), and is based on a trapezoidal shape of the GRACE spacecraft. The drag coefficient and reflectivity was estimated from ranges listed by Wertz and Larson[16] for different spacecraft geometries and materials. The SRP area defines the cross-sectional area of the spacecraft as viewed from the sun and varies over mission lifetime as the Earth orbits the sun and the satellite's orbital plane recesses around the Earth. The satellite flies in a near-polar ($i = 88.5$ deg), near-circular ($\varepsilon = 0.001$) orbit. The range of altitudes considered is 150–450 km.

Table 2 Spacecraft properties and initial conditions

Spacecraft parameters	Value
Mass	487 kg
Drag area	$0.9\ \mathrm{m}^2$
Drag coefficient	2.2
Ballistic coefficient	$246\ \mathrm{kg/m}^2$
SRP area	$0.9–6.1\ \mathrm{m}^2$
Reflectivity coefficient[a]	1.5
Altitude	150–450 km
Eccentricity	0.001
Inclination	88.5 deg
RAAN	0 deg
Argument of perigee	45 deg
True anomaly	180.0 deg

[a] Spacecraft surface assumed to be a diffuse reflector

The drag parameter c includes not only the atmospheric density, but also the ballistic coefficient. In addition to adapting the control response to handle density variations, the adaptive estimate can just as easily handle variations in a spacecraft's ballistic coefficient. For an actual vehicle, the drag area can vary with fluctuations in attitude, the mass will decrease as fuel is consumed, and the drag coefficient will vary based on the molecular constituents and temperature of the atmosphere. Although not explicitly modeled in this study, these changes can also be autonomously accounted for by the adaptation of the controller, allowing the use of constant values for these parameters in the following simulations.

2. *Assumptions*

Several key assumptions were made in the simulations. First, it was assumed that the GRS (and thus the proof mass) is located at the center of mass of the satellite. This assumption eliminates the need for the potentially significant additional ΔV needed to overcome differential orbital velocities (between the proof mass and the spacecraft) resulting from a c.g. offset. The reader is directed to Leitner et al.[8] for a detailed discussion on the topic. We have also neglected any gradients in the "self" gravitation of the spacecraft on the proof mass. These would be nonexistent if the mass distribution of the spacecraft around the proof mass was uniform. In reality this is never the case, but if these deviations from uniformity are sufficiently small, the resulting disturbances will likely be negligible.

Also, it is assumed that the thrusters are oriented in a body-fixed frame that is aligned with the rotating NTW frame of reference described in Sec. II (i.e., the spacecraft longitudinal axis is aligned with the velocity vector). This allows us to isolate the worst-case thrust requirements, as the dominant disturbance (drag) acts only in the direction of the velocity vector.

Finally, it is assumed that there is no initial state error between the proof mass and the spacecraft. The simulation begins when the spacecraft is inserted into the desired orbit, and the GRS is turned on (i.e., the proof mass is uncaged). Any orbital corrections required prior to this time can be performed using the same propulsion system, but using a many-revolution, low-thrust orbit transfer maneuver such as an Alfano transfer.[11]

B. Controller Performance

To initialize the adaptive estimate $\hat{c}$, a determination of the nonconservative forces acting on the spacecraft is needed to enable the usage of a constant adaptive gain Γ. This can be accomplished two ways. First, high-precision accelerometers (as used on the GRACE spacecraft) can be employed before uncaging the proof mass. More convenient, however, would be to obtain the initial drag parameter estimate by operating the GRS in "accelerometer mode." The GRS planned for ST7 and LISA[4] will have this capability, wherein the proof mass is suspended electrostatically while nongravitational forces are measured. In the absence of such information, a "best-guess" initial value for $\hat{c}$ can be used as an input to the controller (based on a high-fidelity atmosphere model, for example), and a time-varying adaptive gain strategy employed within the control law [i.e., $\Gamma = \Gamma(t)$]. This will be necessary to damp out any

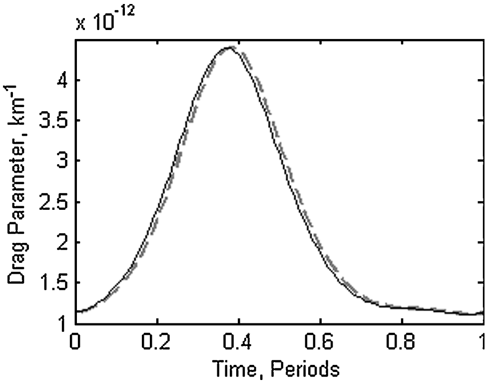

Fig. 3 Adaptive estimate (– – –) compared to actual drag parameter (——) at an altitude of 450 km over one orbital period (94 min). Additional tuning of control gains can further increase the performance of the controller.

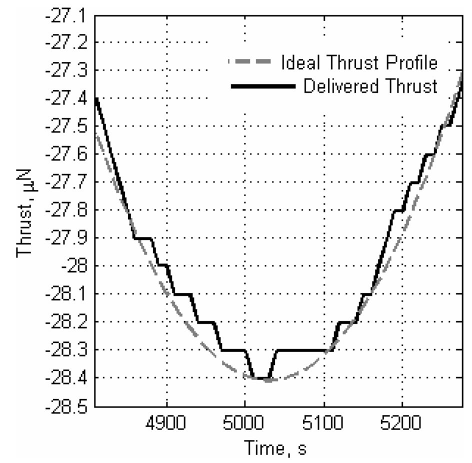

Fig. 4 Detail of partial thrust history for 450 km (with/SRP) shown against ideal value of thrust. Technology constraints limit the deliverability of the thrust to 0.1-μN increments.

initial impulsive thrust spikes that will be commanded by the controller in its attempt to minimize a potentially large drag parameter error.

As noted in Sec. III, if $\hat{c} = c$ exactly, the disturbance from drag will be approximately canceled. In Fig. 3, the evolution of $\hat{c}$ is compared to that of the actual c. It is shown that the adaptive estimate follows the actual drag parameter very closely, except for locations where the time rate of change of the drag parameter, $\dot{c}$, varies significantly. The residual drag disturbance is then handled by the nonlinear and PD components of the controller.

As stated in the Introduction, we assume that the thrust applied for drag compensation is controllable to within a resolution of 0.1 μN. This constraint is incorporated into the spacecraft force model to examine the effects of realistic control/thrust discretization on state error accumulation and thrust requirement. The result of this discretization is seen in Fig. 4, highlighting the fact that the "continuous" cancellation of nongravitational forces is actually discretized not only by the thrust resolution, but also by the control-loop sampling frequency. The actual magnitude of the commanded thrust is shown in Fig. 4 for comparison.

The magnitude to which state errors are allowed to grow will depend in large part on the sampling frequency. In an actual spacecraft, this rate is determined by a number of factors including the sensor hardware and processing power of the onboard computer. In this study, the sampling frequency is not an independent parameter, but rather is determined within the numerical solution by the differential equation solver. In solving the equations of motion (including the applied control acceleration), the ODE23 solver in MATLAB subdivides the integration period into smaller time intervals to maintain a user prescribed accuracy throughout the solution. These internally selected time steps vary depending on the solution gradients and can be interpreted as the equivalent of a control loop sampling period since the control response is updated at each of these steps. For all the cases considered, the equivalent sampling rate was between 0.8 and 31 Hz, which is on the same order as the GRS position sensing rate on ST7.

The following subsections are organized as follows. Case 1 identifies the propulsion requirements for compensation of drag only (SRP is not included) at an altitude of 450 km. In case 2, solar radiation is added to the force model from case 1 to identify any additional requirements that result. Case 3 and 4 are simulated at 250 and 150 km, respectively, also with SRP included. SRP force, however, becomes negligible at these lower altitudes due to the exponential dominance of the drag force perturbation.

C. Case 1: Altitude 450 km

The following plots show a four-period time span on 1 March 2012 for a representative portion of the total 5-year mission. Figure 5 shows the behavior of the position and velocity errors between the spacecraft and the proof mass over the four periods. At 450 km, the state errors are controlled on the order of nanometers and nanometers per second; extremely small, but detectable by a GRS.

Table 3 shows the corresponding maximum state errors along all the NTW components. As expected, the maximum T-component position and velocity errors (4.2 nm and 1.85 nm/s, respectively) are greater than the other components because the disturbing force (drag) acts only in that one direction. The W-component errors are an order of magnitude lower than those of the N and T components, as the out-of-plane component shows less sensitivity to the small thrust values made necessary by the state errors.

Figure 6 shows the thrust profile required for the drag-free operation of a spacecraft at 450 km altitude over the same four orbital periods as in Fig. 5. Over time, the maximum and minimum values for the required thrust will vary because the drag force calculated using the Jacchia–Roberts density model varies with time. Over the lifetime of a 5-year mission, this corresponds to a maximum applied thrust of 136 μN and a minimum applied thrust of 15 μN. This thrust level is positive to counteract the negative pointing drag force. The

Table 3 Maximum state errors at altitude 450 km

Direction	Max. position error, nm	Max. velocity error, nm/s
N	2.56	1.10
T	4.20	1.85
W	0.46	0.37

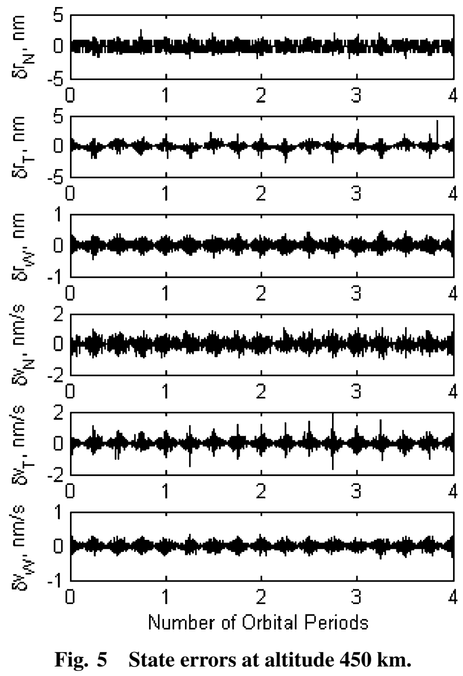

Fig. 5 State errors at altitude 450 km.

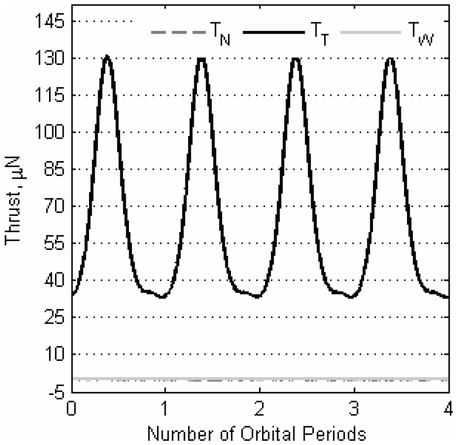

Fig. 6 NTW thrust components over a representative four-period time span at altitude 450 km.

thrust commanded in each of the other two components (the N and W axes) is minimal, limited to a range of -0.4 to $+0.4$ μN.

Because the NTW coordinate system is assumed to be spacecraft-fixed, the spacecraft modeled here is not nadir-pointing. However, because the orbit of the spacecraft is near-circular, the difference between a nadir-pointing attitude and the assumed orientation along the velocity vector is minimal, with a difference in the T- and N-axis thrust components of less than 1% compared with a true nadir-pointing attitude. Alternatively, for GRACE, each spacecraft was actively pointed toward the other spacecraft in the formation.[10] If we adopted the same spacecraft-to-spacecraft pointing attitude used for GRACE, this would have the effect of presenting a slightly larger cross-sectional area for drag forces. For the nominal altitude and in-track offset used on GRACE, this attitude would result in an 11% increase (worst case) over the thrust values reported in this study. Also, because a portion of the top or bottom of the spacecraft (depending on whether the spacecraft is leading or trailing) will be exposed to the oncoming atmosphere, the spacecraft will be subjected to an additional atmospheric force in a direction normal to the velocity vector (i.e., atmospheric lift).

D. Case 2: Effects of Introducing SRP at Altitude 450 km

Unlike atmospheric drag, the disturbing force from SRP does not increase as the altitude of the orbit decreases. In fact, there will be very little change in the SRP force over the range of altitudes explored in this study. Although SRP is included in all of the remaining case studies, the drag force on the satellite becomes exponentially greater at lower altitudes. Thus, the ratio of SRP force over drag force becomes very small, making the effect of SRP on the identification of a mission's propulsion requirement negligible at these lower altitudes. Of the three LEO altitudes we consider in detail, only the highest-altitude case (450 km) shows any noteworthy changes in the overall propulsion requirement due to the inclusion of SRP force.

The high orbital velocity of LEO satellites means that the transition from umbra to penumbra to full illumination occurs over a relatively short time scale. This causes an increase in the required dynamic response of the N- and W-axis thrusters, because they are essentially impulsively perturbed as the satellite moves into, and out of Earth's shadow. For the 450-km altitude case shown in Fig. 7, the passage through penumbra lasts only ~10 s. Also, it is worth noting that the N-axis thrust is mostly positive to counteract the mostly negative-pointing SRP force, with the only exception being short time spans as the satellite moves into and out of penumbra (for the 88.5-deg inclination of the satellite, this occurs over the poles). This is exactly the opposite of the effect of the unmodeled albedo force. As discussed in Sec. II, the albedo force mostly acts radially outward from the Earth along the positive N axis, in opposition to SRP. Hence, the net effect of including the force from Earth's albedo would be to minimize the negative-pointing SRP perturbation along the N axis.

Table 4 Increase in thrust levels for the *N* and *W* components for the 450-km case due to SRP

Direction	Maximum thrust, μN	Mean thrust, μN	Minimum thrust, μN	Max. dynamic response, μN/s
N	40.4	6.7	0	2.35
W	35.1	8.8	0	0.49

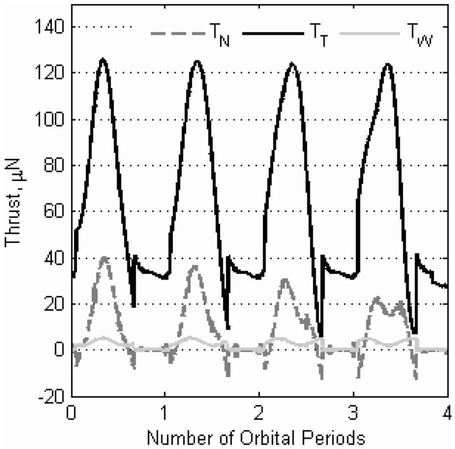

Fig. 7 Thrust profile with addition of SRP at altitude 450 km. The nominal beta angle during this partial thrust history is 16.7 deg.

In addition, we see in Fig. 7 that the SRP force affects each component differently over each orbital period. There are three primary reasons for this. First, as the Earth rotates around the sun, the sun-to-satellite vector changes due to the eccentricity and inclination of the Earth's heliocentric orbit. This seasonal effect results in changes that occur over a relatively large time scale. Second, due to the presence of nonspherical Earth gravitational perturbations, the Keplerian orbit of the spacecraft (and proof mass) will change its orientation with respect to the Earth due to secular regression of the right ascension of the ascending node. Secular drift can cause significant changes to the spacecraft's orientation with respect to the Sun (i.e., cross-sectional area subject to incoming solar flux). These variations occur over a shorter time scale (from orbit to orbit) than seasonal variations, especially for LEO spacecraft. In the four-period thrust history shown, the beta angle range was 16.6–16.9 deg. Finally, short-term variations (within an orbital period) occur throughout the orbit as the fixed attitude of the spacecraft causes it to change orientation of the spacecraft with respect to the sun.

Table 4 shows the increase in the required thrust for the N and W components, as a result of including SRP. The maximum thrust levels represent approximately one-third to one-fourth of the total force from drag at this altitude. The minimum thrust levels for both components are zero, corresponding to the time that the spacecraft is eclipsed by Earth's shadow and the only disturbing force acting on the spacecraft is the drag force. Because these components are essentially shut off during eclipse, however, the maximum dynamic response needed for the radial and out-of-plane components of thrust are increased over the non-SRP (drag-only) simulation. The mean thrust is reported as the time-averaged thrust level.

E. Case 3: Altitude 250 km

Over the same four-period time span at an altitude of 250 km, the behavior of the state errors (Fig. 8) exhibit only slight changes when compared to the 450-km altitude case. In fact, the only component showing a noteworthy increase in state error is the T component, as reported in Table 5. Appearing in the T-component position error at this altitude is a clear, repeated oscillation with period one orbit. This behavior is caused by the build-up of uncorrected drag force, because the disturbance has increased exponentially, but the range of sampling frequencies (0.8–31 Hz) remains relatively unchanged. Because of this error accumulation, the T-component of position and

Table 5 Maximum state errors at altitude 250 km

Direction	Max. position error, nm	Max. velocity error, nm/s
N	2.37	1.05
T	14.16	2.86
W	0.46	0.33

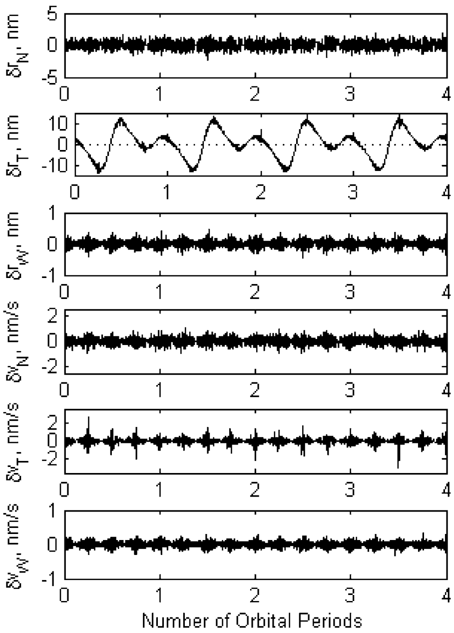

Fig. 8 State errors at altitude 250 km.

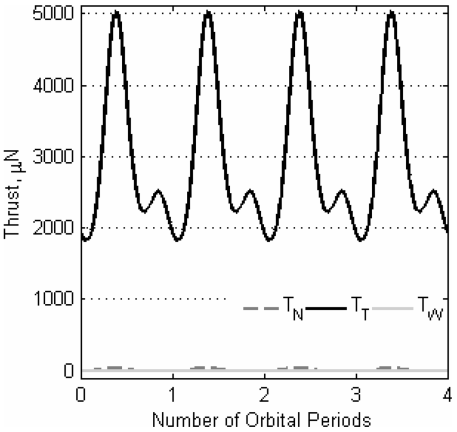

Fig. 9 NTW frame thrust components at $h = 250$ km. The thrust required due to SRP becomes negligible compared to that of the exponentially increasing drag force.

velocity errors increase to 14.16 nm and 2.86 nm/s, respectively. The position error represents an increase of approximately 337%.

At 250 km, the required thrust profile shown in Fig. 9 becomes more severe as the drag force increases exponentially. A dramatic difference between the 450-km case and the 250-km case is the change in the required thrust between apogee and perigee. Within the time span of half an orbital period (~45 min), the thrust must be increased/decreased by approximately 3.3 mN. Over the 5-year mission lifetime, the maximum applied thrust is 5.4 mN and a minimum applied thrust of 1.3 mN. For this lower altitude, we see that the magnitude of the drag force (in the T direction) is much greater than that for the radial and out-of-plane SRP forces. No significant additional requirements are introduced by the inclusion of SRP in the force model.

As noted earlier, no wind model was included in the present calculations. Winds in the thermosphere can be significant, however, and warrant some discussion. The WIND Imaging Interferometer (WINDII) instrument aboard the Upper Atmospheric Research Satellite (UARS) measured neutral winds at altitudes between 90 and 200 km induced by a geomagnetic storm in April 1993.[17] This storm resulted in an increase in the geomagnetic index with peak winds of 650 m/s in the polar region at an altitude of 200 km.

The nominal orbital velocity for the 250-km altitude case presented in this section is 7.90 km/s. If we consider a worst-case head wind of 650 m/s as measured by WINDII at 200 km, the maximum thrust increases to 6.3 mN, a 17% increase. For this same wind speed, the worst-case cross wind (in the cross-track direction) would result in a maximum thrust of approximately 90 μN. This will not alter the choice of propulsion for the in-track thrust component as discussed in Sec. V, but it will likely drive the choice of thruster to provide the cross-track thrust component.

F. Case 4: Altitude 150 km

At 150 km, we see in Fig. 10 that the position error in the T direction exhibits an increasing amount of error accumulation. In fact, the magnitude of this error that is caused by the increasing drag force (for the same range of sampling rate frequency) washes out the controller oscillation. Thus, the position error is increased by an order of magnitude over the 250 km case, with a maximum of 685 nm (Table 6). The other in-plane component (the N component) begins to exhibit this same, low-frequency drag-induced oscillation in addition to higher frequency control oscillations. Even though the drag force acts along only the T axis, the rotation of the coordinate frame means that the alignment of the T axis is continuously changing with time. Therefore, over the coarse of the sampling period, the orientation of the coordinate frame changes slightly, introducing a noticeable error component in the N direction. This effect is present at any altitude, but has become noticeable at 150 km because of the increase in the drag force. Increasing the sampling frequency would tend to reduce the drag-induced effects in the N direction. Unlike the T component, the magnitude of the low-frequency oscillation for the N coordinate is of the same order as the high-frequency controller response. The out-of-plane component, however, changes very little compared with values computed for the 450- and 250-km cases already considered.

Table 6 Maximum state errors at altitude 150 km

Direction	Max. position error, nm	Max. velocity error, nm/s
N	3.09	1.52
T	685	37.4
W	0.38	0.32

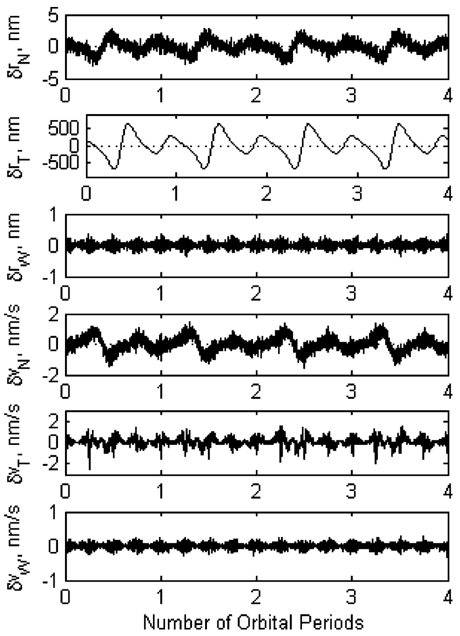

Fig. 10 Displacement and velocity errors at altitude 150 km.

Table 7 Thrust requirements and ΔV over a 5-year mission[a]

Altitude, km	Maximum thrust, μN	Mean thrust, μN	Minimum thrust, μN	Max. dynamic response, μN	ΔV, m/s
150	183,733	77,551	28,579	209.9	25,166
250	5,363	2,651	1,253	6.9	865
450	145	49	10	5.9	20
450 without SRP	136	47	15	2.1	16

[a] Only T component is reported.

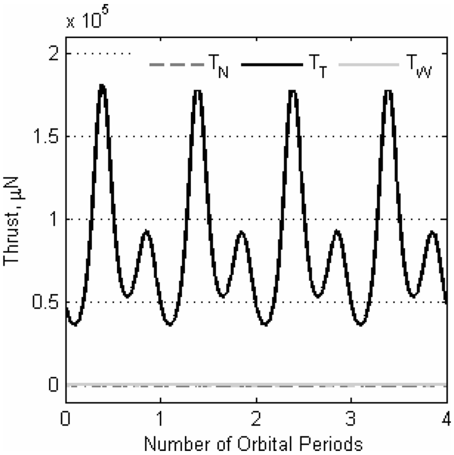

Fig. 11 NTW frame thrust components at altitude 150 km.

Additionally, we observe in Figs. 5, 8, and 10 that the ratio between the T-direction position and velocity errors increases as the altitude is decreased. This is caused primarily by the control system employed. The adaptive term of the controller is strongly dependent on the orbital velocity and the velocity error (due to the presence of the secondary velocity gain γ). The position errors have no such mechanism. Also, due to assumptions made in the development of the adaptive control law (see the Appendix), the controller performs better when adapting to a slowly time-varying drag parameter. Whereas this condition is certainly satisfied for the range of altitudes examined in this study, a more demanding perturbation is presented to the controller at 150-km altitude due to the shorter period and greater magnitude of the disturbance. Additional optimization, or fine-tuning, of the controller gains can be implemented to further decrease the magnitude of these errors.

Compared to the relatively rarified atmosphere at the higher altitudes, the severe atmosphere at 150 km causes significant increases in both the required thrust profile and the dynamic response of the system. From Fig. 11, the maximum required thrust increases to fractions of a newton (~0.2 N), whereas the minimum thrust over the 5-year mission is 29 mN (Table 7). Also significant is the fact that the required thrust must vary over approximately 142 mN between apogee and perigee of a single orbit. From the results reported in Table 7, the amount of this variation alone is orders of magnitude greater than the total maximum thrust for any of the previously discussed cases.

G. Sensitivity of Thrust Level, Thruster Dynamic Response, and ΔV to Altitude

When plotted on a logarithmic scale, we observe in Fig. 12 that the thrust envelope increases from a fractional width standpoint as the altitude increases. That is,

$$(\Delta T/T_{\max})_{450\text{ km}} > (\Delta T/T_{\max})_{150\text{ km}}$$

This result comes directly from the Jacchia–Roberts atmospheric density model that was used in the simulation. As the altitude of the orbit decreases, the variation of the atmospheric density ($\Delta\rho$) decreases due to an assumed constant temperature boundary condition (at an altitude of 90 km) used in developing the thermospheric temperature profile.[13] Therefore, although the magnitude of the thrust variations is much higher at lower altitudes, the density predicted by the Jacchia–Roberts model is less sensitive to changes in the $F_{10.7}$ and a_p at lower altitudes and hence tend to flucuate less.

As the altitude decreases below 250 km, the dynamic response requirement increases exponentially, as shown in Fig. 13. This is caused not only by an exponential increase in the atmospheric density at these lower altitudes, but also by an increase in orbital speed and a decrease in the orbital period of a satellite. As the orbit's altitude is decreased from 450 to 150 km, the spacecraft's orbital speed at perigee is increased by 2.2% and the orbital period is decreased by 6.5%. Hence, the satellite is burdened with overcoming an exponentially increasing drag force in a shorter amount of time.

At altitudes above 250 km, the dynamic response curve shown in Fig. 13 flattens out. This is because at higher altitudes, where the disturbing force due to drag is less, the maximum dynamic response of the thrusters is determined solely by the sampling frequency of the controller. At lower altitudes, the maximum dynamic response is determined by the drag force fluctuations between perigee and apogee of the spacecraft's eccentric orbit. Therefore, if a planned mission is to occupy an orbit with greater eccentricity, the required dynamic response at the lower altitudes will show a significant increase. For comparison, if a true circular orbit is planned, then the dynamic response of the thruster will always be determined by the control-loop response.

Finally, in Fig. 14, we plot the total ΔV for a 5-year mission as a function of altitude. The ΔV is on the order of a kilometer per second at 250 km. The exponential increase is a direct result of the increase in atmospheric density and orbital velocity as the altitude is decreased. These curves were obtained using data points at 50-km altitude intervals.

V. Initial Survey of Thruster Options

In this section we consider some propulsion options to meet the thrust requirements identified for drag-free spacecraft in low Earth orbit. Table 8 lists representative values of thrust-to-power ratio, specific impulse, propellant, and nominal thrust and power for seven different electric propulsion options. For a detailed description of the thruster physics and detailed performance characteristics the reader is referred to the references cited and the references therein. For drag-free spacecraft, the issue of thrust noise (in the bandwidth of interest) is also important. This information is not readily available for most thrusters, although work on ST7 and LISA[4] has contributed to characterizing this noise for some of the FEEP and colloid thrusters. Selection of a propulsion system for any given mission will depend on a number of factors not considered here (technological maturity and development cost, among others). For our purposes here, we will only consider the implications of the thrust envelope, dynamic response, and required ΔV for a 5-year mission at the three altitudes considered. Selection of the specific thruster type and model would be part of a complete trade study once a specific mission is better defined.

The first three thruster technologies listed are the colloid and field emission electric propulsion systems (using indium or cesium fuel). The colloid thruster is part of the Disturbance Reduction System (DRS) experiment package, which will be flown on the NASA New Millennium Program's ST7 Mission. The FEEP thrusters are part of the LISA Technology Package (LTP) under development by the ESA. The DRS, ST7, and LTP will be flown on a European spacecraft carrying both the U.S. and European flight experiments (LISA Pathfinder Mission).[18] The colloid and FEEP are electrostatic thrusters that, in principle, require separate neutralizer cathodes to

Table 8 Performance characteristics for selected thruster options

Thruster	I_{sp}, s	T/P, μN/W	Prop.	Nom. thrust, μN	Peak power, W	Note
Colloid[16]	500–1,500	20	EmI-Im[a]	2–30	1.5	b
In-FEEP[16]	4,000–11,000	15	Indium	2–30	2.0	b
Cs-FEEP[16]	6,000–12,000	17	Cesium	2–30	1.8	b
PPT[17,19]	1150	18	Teflon	50–1,800	100	c
Hall[18]	1370	55	Xenon	1.2–10^4	200	d
Arcjet[19]	500	122	Hydrazine	2.1×10^5–2.5×10^5	1,800	e
Resistojet[19]	300	720	Hydrazine	1.8×10^5–3.6×10^5	500	f

[a] EMI-Im is 1-ethyl-3-methylimidazolium bis(trifluormethylsulfonyl)imide ($C_8H_{11}F_6N_3O_4S_2$).
[b] Based on system under development for ST7 Mission.
[c] Aerojet model PRS-101 thruster. Flown on NASA EO-1 Mission.
[d] Busek model BHT-200 thruster. Originally developed for Air Force Research Lab's TechSat21 Mission.
[e] Aerojet model MR-509 low power arcjet. In production, flight qualified.
[f] Aerojet model MR-501B electrothermal hydrazine thruster. In production, flight qualified.

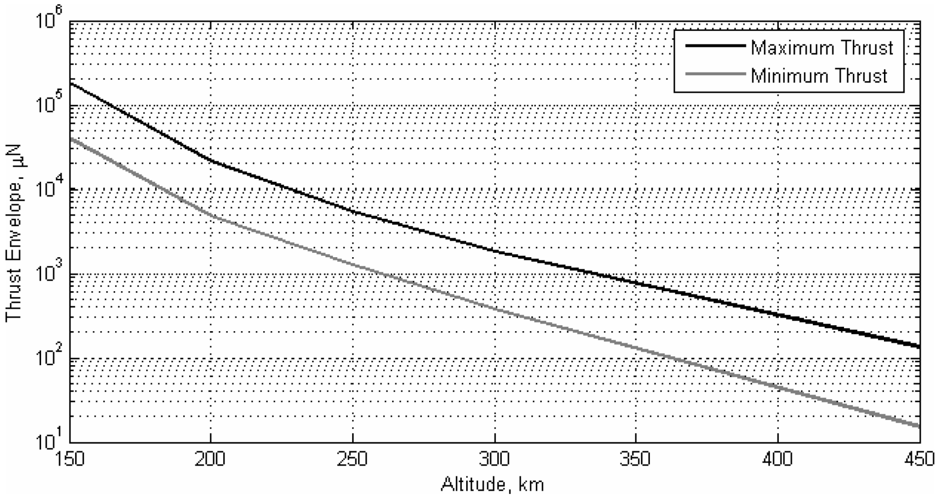

Fig. 12 Required thrust envelope from altitude 150 to 450 km.

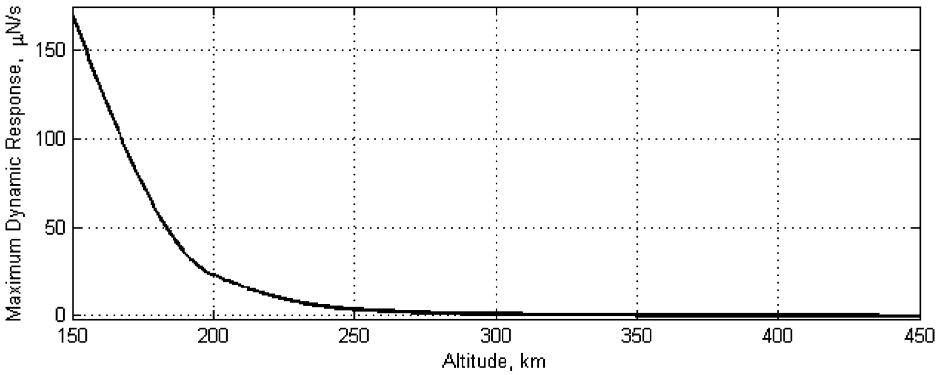

Fig. 13 Maximum required dynamic response over a range of altitudes. Above approximately 250 km, the peak dynamic response is determined by the sampling frequency of the controller. Lower than this, the dynamic response requirement is determined by the drag variations from perigee and apogee.

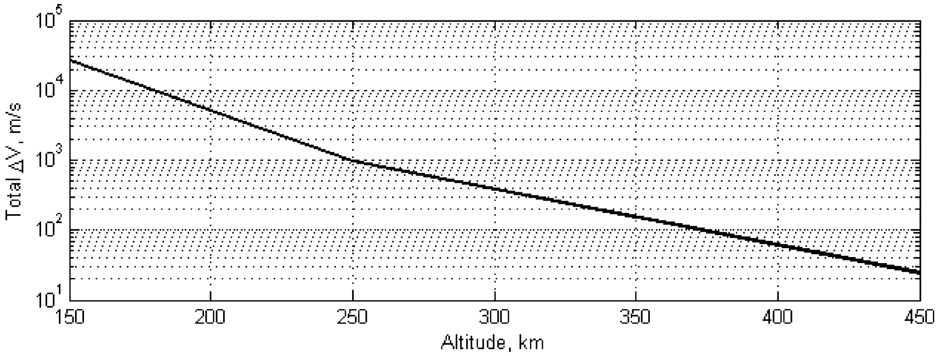

Fig. 14 ΔV requirements for LEO missions over a range of altitudes.

prevent charge from building up on the spacecraft (this requirement may be relaxed somewhat in LEO). Whereas FEEP thrusters are designed to emit primarily ions, colloid thrusters were originally developed to emit charged droplets of a conductive liquid. Sufficiently high conductivity can allow one to operate primarily in an ion-emission regime with an increase in specific impulse and lowering of the thrust-to-power ratio. These three are designed to produce up to 30 μN for ST7 but could be scaled up to provide 150 μN either by using several emitter assemblies or through a combination of additional emitters and higher beam current per emitter.

From Table 7, the required thrust at 450 km ranges from 10 to 145 μN. This thrust range should be achievable with multiple FEEP or colloid thrusters. As noted earlier in the discussion of the thrust history, most of the required thrust, by far, lies in the in-track direction aligned with the velocity vector. The practical implication of this is that a dedicated thruster set to achieve this wide range of thrust can be designed for this one axis, with smaller units along the cross-track and radial directions. The maximum dynamic response required from the thrusters at this altitude is 5.9 μN/s. Adjustment of the thrust at this rate can be accomplished by changing the droplet (or ion in the case of FEEP) accelerating potential. Over the entire range of 10–145 μN, some adjustments would also require changes in flow rate as well. One strategy could be to plan the thrust profile throughout the orbit so that the most rapid throttling will be done through adjustment of the accelerating potential only, with flow rate adjustments made when the required rate (as shown in the thrust history, Fig. 6) is not as high.

The ΔV for the 450-km altitude case, including compensation for solar radiation pressure is approximately 20 m/s over a 5-year mission. Assuming the lowest specific impulse corresponding to a colloid thruster at 500 s, the required propellant would be 2.0 kg. For a 1000-s specific impulse, the propellant mass decreases to 1.0 kg. A FEEP thruster has higher specific impulse (at the cost of lower thrust-to-power ratio) and the propellant mass can be reduced to 0.2 kg for a specific impulse of 4000 s.

The thrust-to-power ratios listed in Table 8 include the power consumption by the neutralizer cathode for the electrostatic thrusters. The projected range of 20–15 μN/W for the colloid and FEEP thrusters results in a required power of 7.3–9.7 W for the maximum thrust of 145 μN listed in Table 7. Even if the required power were doubled to account for charging of batteries (to provide power to propulsion during eclipses), this power requirement is low enough so that it may be possible to rely solely on a body-mounted solar array which helps minimize the ballistic coefficient.

At 250 km, the thrust ranges from 1.3 to 5.4 mN. This is an order of magnitude higher than the peak thrust at 450 km. It is unlikely that the colloid or FEEP thrusters developed for the LISA Pathfinder mission could be adapted for this role without an extensive development effort and re-design. The pulsed plasma thruster (PPT) is an attractive option in this thrust range. The PPT thrust can be adjusted through a combination of changes to the impulse bit (by varying the energy per pulse via the main capacitor) and pulse repetition frequency.[19–22] In Table 8, the nominal thrust range listed corresponds on the low end to a minimum impulse of 50 $\mu\text{N}\cdot\text{s}$ firing at a rate of 1 Hz. The pulse rate could be reduced even lower but at some point the "granularity" will become a limiting constraint. The upper end of the thrust corresponds to an impulse of 825 $\mu\text{N}\cdot\text{s}$ firing at a rate of 2.2 Hz. The peak dynamic response of 6.9 μN/s can also be accommodated through a combination of adjustments in pulse energy and repetition frequency. Maintaining the higher thrust level for extended periods could introduce problems related to capacitor thermal control and lifetime. To achieve the range of 1.3–5.4 mN along the in-track direction would require either multiple thrusters such as the EO-1 PPT listed in Table 8, or the development of a scaled-up thruster.

From a power standpoint, the thrust of 1.3–5.4 mN would require a power of 72–300 W. This large a power requirement (which will likely double when battery charging is included) may require a separate array panel, which will decrease the ballistic coefficient (due to increased area) and worsen the drag acceleration. A much more serious change occurs in the ΔV, which at this altitude increases to 865 m/s for a 5-year mission. This is a substantial ΔV, requiring a propellant mass of 36.1 kg of propellant for a 487-kg wet initial mass. Because our analysis assumed a constant mass (and hence constant ballistic coefficient as well), our results represent a best-case scenario. The required ΔV would increase if the mass change due to propellant consumption were taken into account. Furthermore, 36.1 kg of Teflon corresponds to a delivered impulse of over 405,000 $\text{N}\cdot\text{s}$. This is much greater than the total impulse capability of any existing PPT (3000 $\text{N}\cdot\text{s}$ of impulse for the EO-1 PPT) and would be a significant driver of needed technology development (long-life capacitors, igniters, and electrodes).

Three other alternative thrusters are listed in Table 8. The Hall and arcjet thrusters are low-power versions of these devices. The Hall thruster provides a higher thrust-to-power ratio and specific impulse than the PPT, but some derating or scale-down would be required to operate at one-half to one-fourth the nominal thrust level. With a specific impulse of 1370 s, the Hall thruster would reduce the required propellant mass to 30.4 kg. Furthermore, the need to store gaseous xenon without significantly increasing the surface area imposes additional engineering challenges. The specific impulse of the arcjet and resistojet are considered too low to be viable candidates for a ΔV of 865 m/s.

The third and lowest altitude considered in detail was 150 km. The required thrust range at this altitude is 28.6–184 mN. This range could be accommodated with a cluster of 200-W Hall thrusters, similar to the cluster Busek has been developing with their 600-W thrusters under contract to the Air Force Research Laboratory.[23] The arcjet and resistojet are also candidates from the standpoint of thrust level alone. However, the required ΔV for a 5-year mission is approximately 25 km/s. Even for the Hall thruster's specific impulse of 1370 s, this would require 412.3 kg of propellant mass. From a power standpoint, assuming a thrust-to-power ratio of 55 μN/W for the Hall thruster, over 3 kW would be required, not including power to charge batteries for operation in eclipse. Such a high power requirement would impose a considerable penalty in solar array size and increased drag. We conclude that a 5-year mission duration at 150 km altitude is not likely to be feasible.

We can also consider the question of what range of altitudes is accessible for a given power. We have just seen that the power required for the colloid thruster to produce 145 μN was a modest 7.3 W. Therefore it is likely that the colloid and FEEP thrusters would be limited by thrust rather than power. The arcjet and resistojet, on the other hand, are likely to be limited by specific impulse, so we consider what altitudes would be accessible if one were to use PPT or Hall thrusters within some limited power range. On GRACE, electrical power is provided by four silicon cell arrays located on the satellite top and side surfaces. To estimate the available power, we assume that 80% of the area subject to solar radiation pressure (Table 2) is covered with photovoltaic cells. Furthermore, we assume Ga–As cells with an 18.5% (array) conversion efficiency.[24] Finally, we assume 50% of the total electrical power is available for the propulsion system. For the minimum area listed in Table 2, we therefore estimate the available power to be: $1367\ \text{W/m}^2 \times 0.9\ \text{m}^2 \times 0.185 \times 0.8 \times 0.5 = 91\ \text{W}$. With the maximum area, the available power is 617 W. If we consider the thrust-to-power ratios listed in Table 8, we find this range of power corresponds to 1.6–11.1 mN for the PPT and 5–34 mN for the Hall thruster. Comparing the maximum value of the thrust in each of these ranges with Fig. 12, we see that the PPT thruster may be feasible down to approximately 225 km. The Hall thruster may extend this range down as far as 180 km. Of course, the power system would also have to be able to provide sufficient energy storage to power the thrusters during the eclipse portion of the orbit, and sufficient propellant storage would need to be included to provide the corresponding ΔV from Fig. 14.

VI. Conclusions

The adaptive proportional-derivative control algorithm used in this study has allowed us to determine the required thrust profile and ΔV for drag-free operation of a spacecraft with physical properties representative of a GRACE follow-on mission. The accumulated error in position and velocity was on the order of nanometers and nanometers per second for a controller frequency of 0.8–31 Hz at an altitude of 450 km.

Drag compensation imposes significant demands on the propulsion system, particularly with respect to total impulse requirement for a 5-year mission. At an altitude of 450 km, the colloid or FEEP thrusters should be able to provide the maximum thrust of 145 μN with some additional technology development work to scale up thrusters such as those to be flown on the ST7 Mission. The power and propellant requirements at this altitude are relatively low as well, approximately 7.3 W and 2.0 kg, respectively.

At lower altitudes, the need to minimize the spacecraft surface area may drive one to a more power-limited design. For a maximum available power of 617 W, the PPT thruster may be feasible down to approximately 225 km. This is a significantly higher power than the EO-1 PPT and multiple units along one axis of the spacecraft would probably be required to deliver the peak thrust. At this altitude and below (down to about 180 km) a Hall thruster may be more competitive. A cluster of 200-W thrusters or a single 600-W thruster may be an easier solution than multiple PPTs at altitudes below 250 km. Any complete propulsion trade study also needs to consider propellant storage for a 5-year mission and energy storage during eclipse periods of the near polar orbit.

Finally, we emphasize that the propulsion survey included in this work is intended to be preliminary only. Different thruster technology vendors may have specialized versions of different thrusters under development (high-thrust colloid and PPT, low-power Hall, for example), which could open a range of additional possibilities. The information provided in this paper with respect to thrust level, required thruster dynamic response, and mission ΔV is intended to aid in these continuing studies.

Appendix: Control Design and Stability Analysis

We consider the controlled error equation in Eq. (9) and analyze its stability under various conditions. First, we consider the ideal case in which the exact expression for the drag is known and is given by $\boldsymbol{a}_d(t) = c\hat{\boldsymbol{e}}_v \|\dot{\boldsymbol{r}}_c(t)\|^2$, where $\hat{\boldsymbol{e}}_v$ is defined as the unit vector for the spacecraft velocity relative to the atmosphere. This response forms the ideal case which will serve as the baseline for comparison. We then consider the case of the unknown coefficients of the drag expression (i.e., the constant c is assumed to be an unknown) and implement an adaptive controller that estimates the unknown coefficient c on-line and uses that on-line estimate in the control expression.

A. Ideal Case

By assuming that $\boldsymbol{a}_d(t)$ is known, then the controller for the ideal case is given by

$$\boldsymbol{u}(t) = -\mu\left[\frac{\boldsymbol{r}_t(t)}{\|\boldsymbol{r}_t(t)\|^3} - \frac{\boldsymbol{r}_c(t)}{\|\boldsymbol{r}_c(t)\|^3}\right] - [K_P]\delta\boldsymbol{r}(t) - [K_D]\delta\boldsymbol{r}(t) - c\hat{\boldsymbol{e}}_v\|\dot{\boldsymbol{r}}_c(t)\|^2 \tag{A1}$$

which results in the closed loop error equation

$$\delta\ddot{\boldsymbol{r}}(t) + [K_D]\delta\dot{\boldsymbol{r}}(t) + [K_P]\delta\boldsymbol{r}(t) = \left(\boldsymbol{a}_d - c\hat{\boldsymbol{e}}_v\|\dot{\boldsymbol{r}}_t(t)\|^2\right) = 0 \tag{A2}$$

To analyze the stability of the closed loop system, we may consider the Lyapunov function

$$V(\delta\boldsymbol{r}(t), \delta\dot{\boldsymbol{r}}(t)) = \tfrac{1}{2}\delta\dot{\boldsymbol{r}}^T\delta\dot{\boldsymbol{r}}(t) + \tfrac{1}{2}\delta\boldsymbol{r}^T(t)[K_P]\delta\boldsymbol{r}(t) \tag{A3}$$

which is the sum of the kinetic $[\frac{1}{2}\delta\dot{\boldsymbol{r}}^T(t)\delta\dot{\boldsymbol{r}}(t)]$ and potential energy $[\frac{1}{2}\delta\boldsymbol{r}^T(t)[K_P]\delta\boldsymbol{r}(t)]$ of the closed loop system, and which is positive definite [i.e., $V(\delta\boldsymbol{r}(t), \delta\dot{\boldsymbol{r}}(t)) > 0$] and radially unbounded [i.e., $V(\delta\boldsymbol{r}(t), \delta\dot{\boldsymbol{r}}(t)) \to \infty$ as the norm $\|(\delta\boldsymbol{r}(t), \delta\dot{\boldsymbol{r}}(t))\| \to \infty$]. The latter is guaranteed by the positivity of the Lyapunov function,

$$\begin{aligned} V(\delta\boldsymbol{r}(t), \delta\dot{\boldsymbol{r}}(t)) &= \tfrac{1}{2}\delta\dot{\boldsymbol{r}}^T(t)\delta\dot{\boldsymbol{r}}(t) + \tfrac{1}{2}\delta\boldsymbol{r}^T(t)[K_P]\delta\boldsymbol{r}(t) \\ &\geq \tfrac{1}{2}\|\delta\dot{\boldsymbol{r}}(t)\|^2 + \tfrac{1}{2}\lambda_{\min}([K_P])\|\delta\boldsymbol{r}(t)\|^2 \\ &\geq \tfrac{1}{2}\min\{1, \lambda_{\min}([K_P])\}(\|\delta\dot{\boldsymbol{r}}(t)\|^2 + \|\delta\boldsymbol{r}(t)\|^2) \end{aligned} \tag{A4}$$

To establish the stability of the closed loop system, we evaluate the derivative of the Lyapunov function along the trajectories of the state error system from Eq. (A2):

$$\begin{aligned} \frac{\mathrm{d}}{\mathrm{d}t}V(\delta\boldsymbol{r}(t), \delta\dot{\boldsymbol{r}}(t)) &= \delta\dot{\boldsymbol{r}}^T(t)\delta\ddot{\boldsymbol{r}}(t) + \delta\boldsymbol{r}^T(t)[K_P]\delta\dot{\boldsymbol{r}}(t) \\ &= \delta\dot{\boldsymbol{r}}^T(t)(-[K_P]\delta\boldsymbol{r}(t) - [K_D]\delta\dot{\boldsymbol{r}}(t)) + \delta\boldsymbol{r}^T(t)[K_P]\delta\dot{\boldsymbol{r}}(t) \\ &= -\delta\dot{\boldsymbol{r}}^T(t)[K_D]\delta\dot{\boldsymbol{r}}(t) \leq \lambda_{\min}([K_D])\|\delta\dot{\boldsymbol{r}}(t)\|^2 \leq 0 \end{aligned} \tag{A5}$$

Although the derivative of the Lyapunov function is only negative semidefinite, asymptotic convergence of the error system to zero can still be guaranteed when one makes use of LaSalle's invariance theorem (see Ref. 25). To allow for a more general Lyapunov function that would help with the stability of the adaptive scheme in the second case, we now consider a parameter-dependent Lyapunov function given by

$$\begin{aligned} V_\gamma(\delta\boldsymbol{r}(t), \delta\dot{\boldsymbol{r}}(t)) &= \gamma\frac{1}{2}(\delta\dot{\boldsymbol{r}}^T(t)\delta\dot{\boldsymbol{r}}(t) + \delta\boldsymbol{r}^T(t)[K_P]\delta\boldsymbol{r}(t)) \\ &\quad + \delta\boldsymbol{r}^T(t)\delta\dot{\boldsymbol{r}}(t) + \frac{1}{2}\delta\boldsymbol{r}^T(t)[K_D]\delta\boldsymbol{r}(t) \\ &= \frac{1}{2}[\delta\boldsymbol{r}^T(t) \quad \delta\dot{\boldsymbol{r}}^T(t)]\begin{bmatrix} \gamma[K_P] + [K_D] & I \\ I & \gamma I \end{bmatrix}\begin{bmatrix} \delta\boldsymbol{r}(t) \\ \delta\dot{\boldsymbol{r}}(t) \end{bmatrix} \\ &= \frac{1}{2}[\delta\boldsymbol{r}^T(t) \quad \delta\dot{\boldsymbol{r}}^T(t)]P_\gamma\begin{bmatrix} \delta\boldsymbol{r}(t) \\ \delta\dot{\boldsymbol{r}}(t) \end{bmatrix} \end{aligned} \tag{A6}$$

This modified Lyapunov function can be shown to be positive definite and radially unbounded when the parameter $\gamma > 0$ is chosen sufficiently large via

$$\gamma > \max\left\{1, \frac{1 - \lambda_{\min}[K_D]}{\lambda_{\min}[K_P]}, \frac{1}{\lambda_{\min}[K_D]}\right\} \tag{A7}$$

Using the symmetry of the diagonal matrices $[K_D]$ and $[K_P]$, the derivative of $V_\gamma(\delta\boldsymbol{r}(t), \delta\dot{\boldsymbol{r}}(t))$ is then given by

$$\begin{aligned} \frac{\mathrm{d}}{\mathrm{d}t}V_\gamma(\delta\boldsymbol{r}(t), \delta\dot{\boldsymbol{r}}(t)) &= \gamma\left(\delta\dot{\boldsymbol{r}}^T(t)\delta\ddot{\boldsymbol{r}}(t) + \delta\boldsymbol{r}^T(t)[K_P]\delta\dot{\boldsymbol{r}}(t)\right) \\ &\quad + \delta\boldsymbol{r}^T(t)\delta\ddot{\boldsymbol{r}}(t) + \|\delta\dot{\boldsymbol{r}}(t)\|^2 + \delta\boldsymbol{r}^T(t)[K_D]\delta\dot{\boldsymbol{r}}(t) \\ &= \gamma\delta\dot{\boldsymbol{r}}^T(t)[K_D]\delta\dot{\boldsymbol{r}}(t) - \delta\boldsymbol{r}^T(t)[K_P]\delta\boldsymbol{r}(t) + \|\delta\dot{\boldsymbol{r}}(t)\|^2 \\ &= -(\gamma\lambda_{\min}([K_D]) - 1)\|\delta\dot{\boldsymbol{r}}(t)\|^2 - \lambda_{\min}([K_P])\|\delta\boldsymbol{r}(t)\|^2 \\ &\leq -\min\{\lambda_{\min}([K_P]), \gamma\lambda_{\min}([K_D]) - 1\}\left[\|\delta\boldsymbol{r}(t)\|^2 + \|\delta\dot{\boldsymbol{r}}(t)\|^2\right] \\ &\leq -\alpha V_\gamma(\delta\boldsymbol{r}(t), \delta\dot{\boldsymbol{r}}(t)) \end{aligned} \tag{A8}$$

for some positive parameter α which depends on the bound γ. Using the preceding, one can conclude on the exponential stability of the system, i.e., that the state position and state velocity errors will converge to zero exponentially.

B. Adaptive Controller

We now consider the case in which the drag parameter c is not known and must therefore be estimated on line. Toward that end, we propose the following adaptive controller, which is given by the control law

$$\boldsymbol{u}(t) = -\mu\left[\frac{\boldsymbol{r}_t(t)}{\|\boldsymbol{r}_t(t)\|^3} - \frac{\boldsymbol{r}_c(t)}{\|\boldsymbol{r}_c(t)\|^3}\right] - [K_P]\delta\boldsymbol{r}(t) - [K_D]\delta\dot{\boldsymbol{r}}(t) - \hat{c}(t)\hat{\boldsymbol{e}}_v(t)\|\dot{\boldsymbol{r}}_c(t)\|^2 \tag{A9}$$

where $\hat{c}(t)$ denotes the adaptive estimate of the unknown c, and the parameter update law is defined as

$$\frac{\mathrm{d}}{\mathrm{d}t}\hat{c}(t) = -\Gamma(\gamma\delta\dot{\boldsymbol{r}}(t) + \delta\boldsymbol{r}(t))^T\hat{\boldsymbol{e}}_v(t)\|\dot{\boldsymbol{r}}_c(t)\|^2 \tag{A10}$$

The adaptive gain $\Gamma > 0$ is a design parameter chosen as a positive scalar the purpose of which is to affect the speed of adaptation.

The closed loop system with this control law becomes

$$\begin{aligned}\delta\ddot{\boldsymbol{r}}(t) + [K_D]\delta\dot{\boldsymbol{r}}(t) + [K_P]\delta\boldsymbol{r}(t) &= \left(\boldsymbol{a}_d - \hat{\boldsymbol{c}}(t)\hat{\boldsymbol{e}}_v(t)\|\dot{\boldsymbol{r}}_c(t)\|^2\right)\\ &= (c - \hat{c}(t))\hat{\boldsymbol{e}}_v(t)\|\dot{\boldsymbol{r}}_c(t)\|^2 = \tilde{c}(t)\hat{\boldsymbol{e}}_v(t)\|\dot{\boldsymbol{r}}_c(t)\|^2 \end{aligned}\tag{A11}$$

where $\tilde{c}(t) = c - \hat{c}(t)$ denotes the drag parameter error. To analyze the stability of the adaptive system, we consider the Lyapunov function $V_\gamma(\delta\boldsymbol{r}(t), \delta\dot{\boldsymbol{r}}(t))$ modified to include the parameter error and therefore given by

$$\begin{aligned}V_\gamma(\delta\boldsymbol{r}(t), \delta\dot{\boldsymbol{r}}(t), \tilde{c}(t)) &= \gamma\tfrac{1}{2}\left(\delta\dot{\boldsymbol{r}}^T(t)\delta\dot{\boldsymbol{r}}(t) + \delta\boldsymbol{r}^T(t)[K_P]\delta\boldsymbol{r}(t)\right)\\ &\quad + \delta\boldsymbol{r}^T(t)\delta\dot{\boldsymbol{r}}(t)\tfrac{1}{2}\delta\boldsymbol{r}^T(t)[K_D]\delta\boldsymbol{r}^T(t) + \tfrac{1}{2}\Gamma\tilde{c}^2(t)\end{aligned}\tag{A12}$$

One can easily show that the modified Lyapunov function is positive definite and radially unbounded. To examine the stability of the system and its adaptive control, we evaluate the derivative of the Lyapunov function along the trajectory of the error system from Eq. (A11):

$$\begin{aligned}\frac{\mathrm{d}}{\mathrm{d}t}V_\gamma(\delta\boldsymbol{r}(t), \delta\dot{\boldsymbol{r}}(t), \tilde{c}(t)) &= \gamma\left(\delta\dot{\boldsymbol{r}}^T(t)\delta\ddot{\boldsymbol{r}}(t) + \delta\boldsymbol{r}^T(t)[K_P]\delta\dot{\boldsymbol{r}}(t)\right)\\ &\quad + \delta\boldsymbol{r}^T(t)\delta\ddot{\boldsymbol{r}}(t) + \|\delta\dot{\boldsymbol{r}}(t)\|^2 + \delta\boldsymbol{r}^T(t)[K_D]\delta\dot{\boldsymbol{r}}(t) + \tfrac{1}{2}\Gamma\dot{\tilde{c}}(t)\tilde{c}(t)\\ &= \gamma\delta\dot{\boldsymbol{r}}^T(t)[K_D]\delta\dot{\boldsymbol{r}}(t) - \delta\boldsymbol{r}^T(t)[K_P]\delta\dot{\boldsymbol{r}}(t) + \|\delta\dot{\boldsymbol{r}}(t)\|^2\\ &\quad + \left(\gamma\delta\dot{\boldsymbol{r}}^T(t)\boldsymbol{w}\|\delta\dot{\boldsymbol{r}}(t)\|^2 + \delta\boldsymbol{r}^T(t)\hat{\boldsymbol{e}}_v\|\delta\dot{\boldsymbol{r}}(t)\|^2 + (1/\Gamma)\dot{\tilde{c}}(t)\right)\tilde{c}(t)\\ &= -\left(\gamma\lambda_{\min}([K_D]) - 1\right)\|\delta\dot{\boldsymbol{r}}(t)\|^2 - \lambda_{\min}([K_P])\|\delta\boldsymbol{r}(t)\|^2\\ &\le -\min\left\{\lambda_{\min}([K_P]), \gamma\lambda_{\min}([K_D]) - 1\right\}[\|\delta\boldsymbol{r}(t)\|^2\\ &\quad + \|\delta\dot{\boldsymbol{r}}(t)\|^2] \le 0\end{aligned}\tag{A13}$$

Unlike the nonadaptive case, this Lyapunov function has a negative semidefinite derivative and hence asymptotic stability cannot be inferred. However, following rather standard results in adaptive estimation and control theory, one may use Barbălat's lemma (see Ref. 25) and show asymptotic convergence of the state position and state velocity errors, and boundedness of the adaptive estimate $\hat{c}(t)$ of the unknown c. To establish parameter convergence in the sense of $\lim_{t\to\infty}\tilde{c} = 0$, one must further impose the condition of persistence of excitation on the control signal.

Acknowledgments

The authors thank William Folkner of NASA's Jet Propulsion Laboratory and Tim Velegol of A. I. Solutions, Inc., for their valuable suggestions and assistance.

References

[1] Genovese, A., Steiger, W., and Tajmar, M., "Indium FEEP Microthruster: Experimental Characterization in the 1–100 μN Range," AIAA Paper 2001-3788, July 2001.

[2] Marcuccio, S., Ciucci, A., Oest, H., Genovese, A., and Andrenucci, M., "Flight Demonstration Opportunities for FEEP," AIAA Paper 96-2724, July 1996.

[3] Hruby, V., Gamero-Castaño, M., Falkos, P., and Shenoy, S., "Micro Newton Colloid Thruster System Development," International Electric Propulsion Conf., IEPC-01-281, Oct. 2001.

[4] Bender, P., Brillet, A., Ciufolini, I., Cruise, A. M., Cutler, C., Danzmann, K., Fidecaro, F., Folkner, W. M., Hough, J., McNamara, P., Peterseim, M., Robertson, D., Rodrigues, M., Rüdiger, A., Sandford, M., Schäfer, G., Schilling, R., Schutz, B., Speake, C., Stebbins, R. T., Sumner, T., Touboul, P., Vinet, J. Y., Vitale, S., Ward, H., and Winkler, W., "LISA: Laser Interferometer Space Antenna, Pre-Phase A Report," 2nd ed., MPQ-233, LISA Study Team, Max-Planck Inst., Potsdam, Germany, July 1998.

[5] Turneaure, J. P., Everitt, C. W. F., Parkinson, B. W., Bardas, D., and Breakwell, J. V., "The Gravity-Probe-B Relativity Gyroscope Experiment—Development of the Prototype Flight Instrument," *Advances in Space Research*, Vol. 9, No. 9, 1989, pp. 29–38.

[6] Centre National d'Etudes Spatiales, "The MICROSCOPE Mission Begins," Press Release PR38-2004, June 2004, URL: http://www.cnes.fr/html/_455_465_2424_.php [cited 14 Jan. 2005].

[7] Watkins, M. M., Folkner, W. M., Chao, B. F., and Tapley, B. D., "The NASA EX-5 Mission: A Laser Interferometer Mission Follow-On to GRACE," Gravity, Geoid, and Geodynamics 2000 International Symposium, International Association of Geodesy, July–Aug. 2000.

[8] Leitner, J., Starin, S., Fleck, M., Naasz, B., and Fall, R., "Investigation of Drag-Free Control Technology for Earth Science Constellation Missions," NASA Earth Science Technology Office, Final Rept., May 2003.

[9] Kim, J., and Tapley, B. D., "Error Analysis of a Low–Low Satellite-to-Satellite Tracking Mission," *Journal of Guidance, Control, and Dynamics*, Vol. 25, No. 6, 2002, pp. 1100–1106.

[10] NASA, "GRACE Launch Press Kit," March 2002, p. 18.

[11] Vallado, D. A., *Fundamentals of Astrodynamics and Applications*, Space Technology Library, Microcosm Press, El Segundo, CA, 2001, Chap. 8.

[12] Montenbruck, O., and Gill, E., *Satellite Orbits: Models, Methods, and Applications*, Springer-Verlag, Berlin, 2000, pp. 83–86.

[13] Roberts, C., "An Analytical Model for Upper Atmosphere Densities Based upon Jacchia's 1970 Models," *Journal of Celestial Mechanics*, Vol. 4, No. 3, 1971, pp. 368–377.

[14] Schatten, K. H., "Solar Activity and the Solar Cycle," *Advances in Space Research*, Vol. 32, No. 4, 2003, pp. 451–460.

[15] Chao, C. C., Gunning, G. R., Moe, K., Chastain, S. H., and Settecerri, T. J., "Evaluation of Jacchia 71 and MSIS90 Atmosphere Models with NASA ODERACS Decay Data," *Journal of the Astronautical Sciences*, Vol. 45, No. 2, 1997, pp. 131–141.

[16] Wertz, J. R., and Larson, W. J., *Space Mission Analysis and Design*, 3rd ed., Space Technology Library, Microcosm Press, El Segundo, CA, 1999, Chap. 8.

[17] Zhang, S. P., and Shepherd, G. S., "Neutral Winds in the Lower Thermosphere Observed by WINDII During the April 4–5th, 1993 Storm," *Geophysical Research Letters*, Vol. 27, No. 13, 2000, pp. 1855–1858.

[18] Ziemer, J. K., and Merkowitz, S. M., "Microthrust Propulsion for the LISA Mission," AIAA Paper 2004-3439, July 2004.

[19] Blandino, J. J., Cassady, R. J., and Peterson, T. T., "Pulsed Plasma Thrusters for the New Millennium Interferometer (DS-3) Mission," 25th International Electric Propulsion Conf., IEPC 97-192, Aug. 1997.

[20] Blandino, J. J., and Cassady, R. J., "Propulsion Requirements and Options for the New Millennium Interferometer (DS-3) Mission," AIAA Paper 98-3331, July 1998.

[21] Cassady, R. J., Willey, M. J., Meckel, N. J., and Blandino, J. J., "Pulsed Plasma Thruster for the New Millennium Space Interferometer Experiment DS-3," AIAA Paper 98-3326, July 1998.

[22] Tilley, D. L., Pobst, J. A., Bromaghim, D. R., Myers, R. M., Cassady, R. J., Hoskins, W. A., Meckel, N. J., Blandino, J. J., Brinza, D. E., and Henry, M. D., "Advanced Pulsed Plasma Thruster Demonstration on MightySat Flight II.1," AIAA/Utah State Univ. Conf. on Small Satellites, Sept. 1996.

[23] Hruby, V., "Review of Electric Propulsion Activities in the US Industry," AIAA Paper 2003-4441, July 2003.

[24] "Space Systems Capabilities and Technologies," Product Catalog, 99-H-2548, Primex Aerospace Co. (now Aerojet), 1999.

[25] Ioannou, P. A., and Sun, J. H., *Robust Adaptive Control*, Prentice–Hall, New York, 1995, Chap. 2.

N. Gatsonis
Associate Editor